CCS Chemistry

RESEARCH ARTICLE

Received: Dec. 4, 2018 | Accepted: July 1, 2019 | Published: Oct. 4, 2019

Photoresponsive Biomimetic Protocells for Near-Infrared-Light-Regulated Phototheranostics

Ling Liang[1†], Yawei Tang[1†], Xiaoxiao Hu[1†], Jie Wang[2], Shehua Xiao[1], Dan Li[1], Linna Fu[1], Zhihao Li[2] & Quan Yuan[1,2*]

[1]*Molecular Science and Biomedicine Laboratory, Institute of Chemical Biology and Nanomedicine, State Key Laboratory of Chemo/Biosensing and Chemometrics, College of Chemistry and Chemical Engineering, College of Life Sciences, and Aptamer Engineering Center of Hunan Province, Hunan University, Changsha 410082 (China),* [2]*Key Laboratory of Analytical Chemistry for Biology and Medicine (Ministry of Education), College of Chemistry and Molecular Sciences, Wuhan University, Wuhan 430072 (China)*

**Corresponding author: yuanquan@whu.edu.cn;* [†]Liang, Tang, and Hu contributed equally to this work

Cite this: *CCS Chem.* **2019**, *1*, 490–501

Nature has created complex living systems with outstanding structure and remarkable function. Constructing biomimetic systems that rival living organisms has attracted considerable research interest in research fields of self-assembly and bionic science. Inspired by the composition of photosynthetic bacteria, we have designed artificial photoresponsive protocells through capsulation of upconversion nanoparticles@black phosphorus quantum dots (UCNPs@BPQDs) within aptamer-modified liposome (Apt-Lip) to form UCNPs@BPQDs@Apt-Lip (UBAL). The UBAL protocells with near-infrared-light-harvesting capability actively and efficiently convert light energy into chemical and heat energy. Furthermore, the successful application of the protocells to malignant tumors in vivo exhibited near-infrared-light-mediated targeted combined photodynamic and photothermal synergistic therapy. Our demonstration of operative protocells not only represents a method for fabricating light-harvesting systems based on nanoassembly, but also provides a promising step toward photosynthetic protocells with integrated cell-like structure and light-harvesting function for nanomedicine.

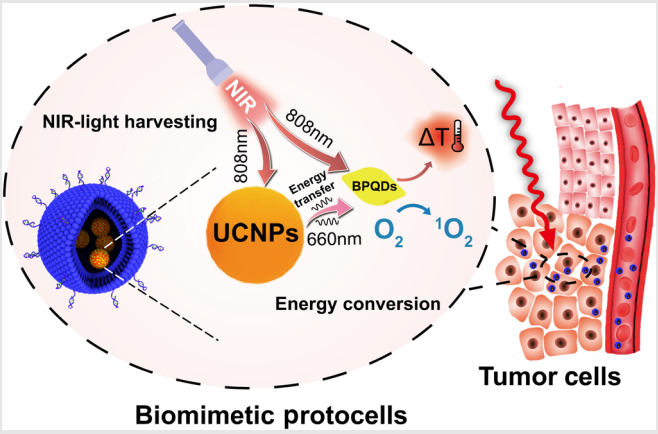

Keywords: **aptamer, upconversion, black phosphorus, near-infrared light, bioimaging**

Introduction

The biological world has evolved to produce a wide variety of intelligent biomaterials that often have elaborate hierarchical structural assemblies arising from weakly interacting, yet readily available building blocks.[1,2] Inspired by such natural systems, constructing an intelligent system that rivals the structure and function of living organisms has attracted enormous research interest in self-assembly and bionic science.[3–5] Photosynthetic bacteria, one of the simplest single-celled organisms, use light energy for photosynthesis and metabolism.[6–8] They can absorb photons on the submicron scale and efficiently convert light energy into accessible

DOI: 10.31635/ccschem.019.20180033
CCS Chem. **2019**, *1*, 490–501

chemical energy. Photosynthetic-bacteria-inspired studies have attracted increasing attention, challenging researchers to improve the ability to manipulate photons[9,10] and develop more precise and efficient energy transfer pathways.[11,12] The construction of functional nanomaterials that mimic photosynthetic bacteria holds great promise in areas associated with energy conversion,[13-15] optoelectronics,[16,17] and nanomedicine.[18-21]

The photosynthesis center of photosynthetic bacteria is located around the light-harvesting antenna formed by self-assembled pigments.[7,22] The hydrophobic cell membranes provide a relatively stable environment for photosynthesis.[22] The most important process in the natural photosynthetic system is the absorption of sunlight by light-harvesting complexes and the subsequent transport of the absorbed photons to photosynthetic reaction centers.[12] Hierarchical assembly is thus the main strategy for the construction of an artificial photosynthetic system,[23,24] and researchers have fabricated numerous photosynthesis models for the conversion of light energy to chemical energy.[25-30] The photosynthetic substance could be assembled on a carrier that allows the harvested energy to be quickly and efficiently transferred to the photosynthetic reaction center. However, the conformation of light-harvesting molecules[10,31,32] and the stability of the photosynthetic reaction center[23,33,34] are influenced significantly by the surrounding environment. As a next step, researchers have encapsulated the carriers into a more stable system, such as micelles, to form synthetic cell-like structures.[28,35] Although the structural and functional biomimetics have been challenging, incredible effort continues to be undertaken to construct assembly systems with structure and function that mimic photosynthetic bacteria due to the carryover of this research into bioelectronics, catalysis, and medicine.

Herein, we designed artificial photoresponsive protocells that mimic the structure and light-harvesting function of photosynthetic bacteria for imaging-guided combined photodynamic and photothermal therapy (Figure 1). The photoresponsive protocells were constructed by encapsulating core-satellite-structured upconversion nanoparticles@black phosphorus quantum dots (UCNPs@BPQDs) into aptamer-modified liposomes (Apt-Lip) to form UCNPs@BPQDs@Apt-Lip (UBAL) protocells. In the protocells, the UCNPs-absorbed near-infrared (NIR) light and transferred energy to BPQDs, leading to the transition of the ground state electrons of BPQDs to the excited state. The excited electrons then transferred their energy to oxygen molecules to generate singlet oxygen ($^1O_2$).[36-38] Meanwhile, BPQDs could absorb NIR and generate heat.[39-41] With the above structure and function, the UBAL protocells could absorb light strongly and convert the light energy into chemical and heat energy efficiently for imaging-guided

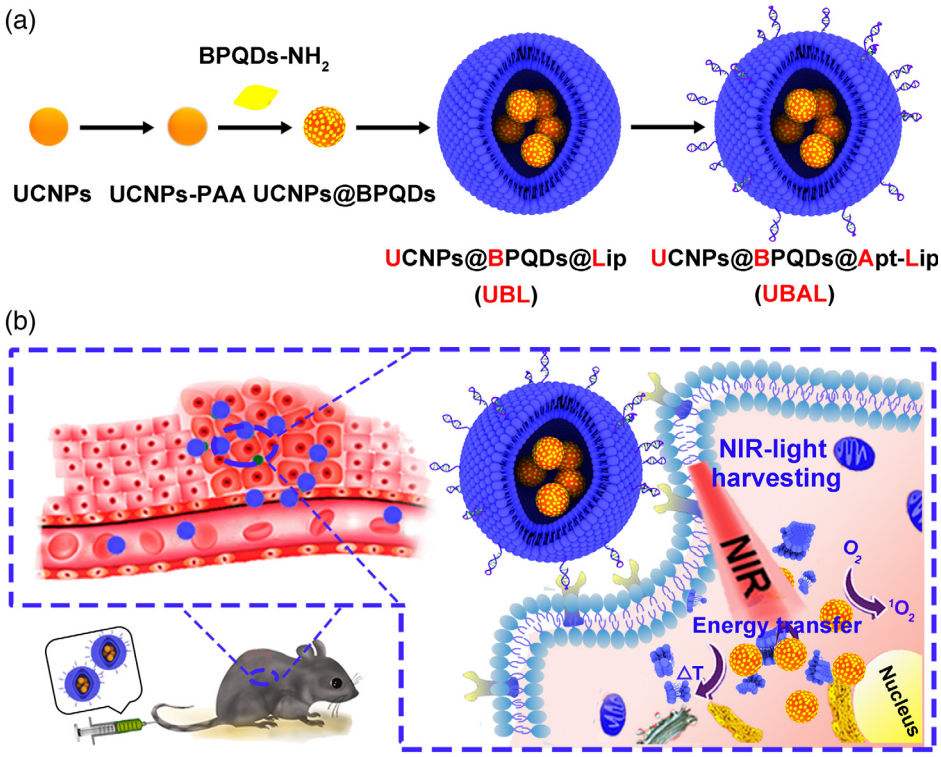

Figure 1 | *(a) Schematic representation of the fabrication process of the hierarchically assembled UBAL protocells. (b) Illustration of the UBAL protocells that absorb light strongly and efficiently convert light energy into chemical and heat energy for NIR-light-mediated in vivo targeted phototheranostics.*

DOI: 10.31635/ccschem.019.20180033
CCS Chem. **2019**, *1*, 490–501

photodynamic and photothermal therapy. Our newly fabricated protocells are thus expected to offer several benefits: First, the NIR-light-harvesting system could capture long-wavelength NIR light, which accounts for more than 50% of sunlight. We took advantage of UCNPs which have the ability to convert NIR light to ultraviolet and visible light by sequential absorption of photons.[42–45] Herein, we fabricated artificial photoresponsive protocells that could assist the harvesting of long-wavelength NIR light. Secondly, as the current available NIR-light-harvesting system mainly focuses on dye-sensitized solar cells[46] and photoenzymatic catalysis,[47] we envisioned that this NIR-light-harvesting system could expand its application in nanomedicine due to its high sensitivity and resolution, as well as the deep-tissue permeability of NIR light. Finally, in addition to the structural and light-harvesting function similarity to photosynthetic bacteria, protocells with aptamer also possess strong binding affinity and high selectivity toward their targets.[48,49] Therefore, our demonstration of protocells not only represents a method for fabricating light-harvesting systems based on nanoassembly, but it also provides a promising step towards artificial photosynthetic protocells with integrated cell-like structure and light-harvesting function for nanomedicine.

Results and Discussion

Design and characterization of multifunctional photoresponsive protocells

Figure 1a illustrates the preparation of the photoresponsive UBAL protocells via encapsulation of core-satellite-structured UCNPs@BPQDs within Apt-Lip. Briefly, the core–shell UCNPs were synthesized (Supporting Information Figures S1–S4) in order to avoid an environmental quenching effect and to enhance the sensitization of oxidized neodymium (Nd^{3+}) with high upconversion efficiency under 808 nm irradiation. These UCNPs were further coated with poly(acrylic acid) (PAA) (Supporting Information Figures S5–S7) by a ligand-exchange procedure to facilitate subsequent surface modification. The ultrasmall BPQDs were synthesized (Supporting Information Figures S8 and S9) by the liquid exfoliation method from bulk crystals, and amino-groups-modification of BPQDs (BPQDs-NH_2) was achieved through electrostatic adsorption of amino-terminated polyethylene glycol (Supporting Information Figure S10). Then, the BPQDs-NH_2 were hierarchically assembled on the surface of PAA-coated UCNPs (UCNPs-PAA), resulting in the fabrication of UCNPs@BPQDs with the aid of the well-known 1-[3-(dimethylamino)propyl]-3-ethylcarbodiimide hydrochloride (EDC)/ N-hydroxysuccinimide (NHS) chemistry. Subsequently, the prepared UCNPs@BPQDs were mixed with maleimide-functionalized liposomes (Mal-Lip) (Supporting Information Figure S11 and Table S1) in a 37 °C bath, leading to an aqueous core UCNPs@BPQDs-encapsulated liposome reconstruction. Finally, the UBAL protocells were successfully fabricated by thiol-maleimide cross-linking chemistry between 3′-thiol-modified aptamer and Mal-Lip.

The structure of UCNPs@BPQDs was characterized as follows: (1) Transmission electron microscopy (TEM) images showed the presence of BPQDs on the surface of UCNPs, and the composite maintained good dispersity (Supporting Information Figure S12). (2) Scanning transmission electron microscopy (STEM) images (Figure 2a,b) further confirmed the formation of UCNPs@BPQDs core-satellite structure. (3) Functionalization steps were verified by dynamic light scattering and Fourier-transform infrared spectroscopy; UCNPs-PAA was negatively charged (–17.4 mV) because of the carboxyl group in PAA, and UCNPs@BPQDs had a greater negative charge of –27.2 mV (Supporting Information Figure S13). The UCNPs@BPQDs displayed two vibrational peaks at around 1647 and 1566 cm^{-1} (Supporting Information Figure S14), which were attributed to the asymmetric stretching mode of the imidoyl group and the amide vibrations. These results indicate the successful conjugation of BPQDs to UCNPs. (4) The *Y/P* molar ratio was measured to quantify the total amount of BPQDs conjugated onto the surface of UCNPs by inductively coupled plasma mass spectrometry measurements[50] (Supporting Information Table S2). The latter result shows that the *Y/P* molar ratio is to be 100:96.5 in UCNPs@BPQDs nanostructure (P content 13.7 wt %), indicating that 159 μg of BPQDs conjugated onto the surface of per milligrams of UCNPs. (5) According to the average particle sizes of UCNPs and BPQDs from TEM images and the density from X-ray diffraction, the number of BPQDs per one UCNPs was calculated to be 20.

Encapsulation of UCNPs@BPQDs in the liposome was further investigated as follows: The TEM images at different magnification (Figure 2c and Supporting Information Figure S15) showed the uniform spherical structure of UBAL with a diameter ranging from 100 to 200 nm. The protocell structure of UBAL was identified as an appearance of UCNPs@BPQDs in the core of the liposome. Atomic force microscopy (AFM) images also showed a spherical morphology of UBAL, and the measured heights were about 50 nm (Figure 2d,e). Micrometer-scaled UBAL was further fabricated to confirm the formation of protocell structure,[51] which was subsequently characterized using laser scanning confocal microscope (LSCM). Green fluorescence signals from FAM-labeled Apt-Lip under the excitation of 488 nm laser, and the red luminescence signals from UCNPs@BPQDs under the two-photon LSCM (808 nm laser) were observed (Figure 2f). The merged image clearly showed that the UCNPs@BPQDs colocalized with FAM-labeled Apt-Lip, indicating the successful loading of UCNPs@BPQDs into Apt-Lip. The stability of protocell

DOI: 10.31635/ccschem.019.20180033
CCS Chem. **2019**, *1*, 490–501

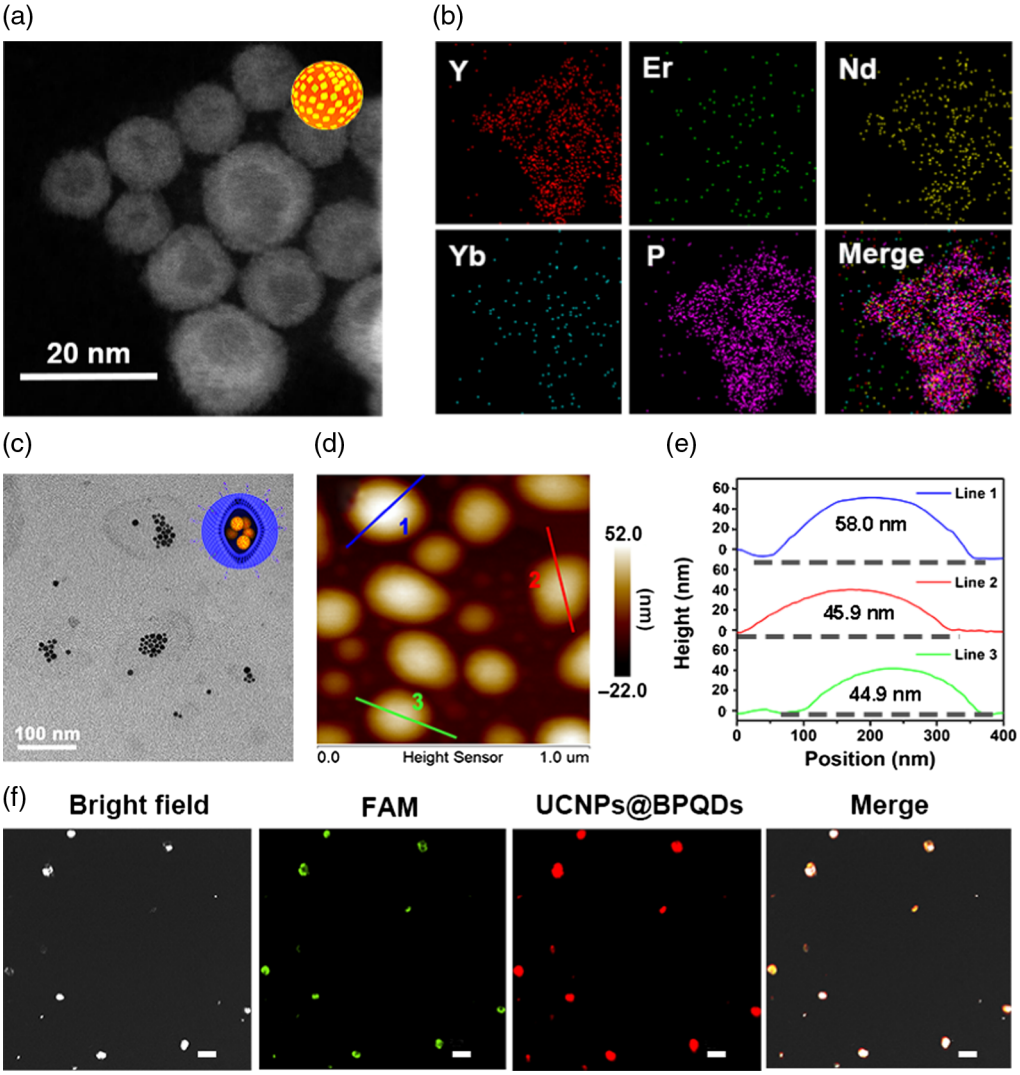

Figure 2 | *Characterization of UBAL protocells. (a and b) STEM image with the elemental mapping images of UCNPs@BPQDs. (c) The TEM image of UBAL protocells. (d and e) AFM image of the UBAL protocells and the height profiles along the lines. (f) Fluorescence images of UBAL protocells with bright-field, FAM-labeled Apt-Lip, UCNPs@BPQDs, and merge image. Scale bars, 5 μm.*

structure was further characterized by dynamic light scattering and cargo release profiles (Supporting Information Figure S15). The time-dependent size remains unchanged and a constant release rate shows a limited leakage, implying the good stability of UBAL protocells. Collectively, these results suggest that UBAL protocells were constructed successfully with the bottom-up assembly strategy.

Photoresponse performance and selective recognition function of UBAL

The photoresponse performance and the upconversion resonance energy transfer of the UBAL protocells were further investigated (Figure 3a). The emissions at 409, 520–570, and 650–690 nm of UCNPs under 808 nm laser excitation were assigned to the respective $^2H_{9/2} \rightarrow {}^4I_{15/2}$, $^2H_{11/2}/{}^4S_{3/2} \rightarrow {}^4I_{15/2}$, and $^4F_{9/2} \rightarrow {}^4I_{15/2}$ transitions of Er^{3+} ions.[52] The role of the Yb^{3+} ions across the core–shell interface was to initiate $Nd^{3+} \rightarrow Yb^{3+} \rightarrow Er^{3+}$ energy transfer and to tune the optical emission of Er^{3+} ions.[53] Figure 3b shows the upconversion luminescence spectrum of the UCNPs-PAA and UBAL protocells, following excitation with 808 nm laser. As expected, the absorption spectrum of BPQDs exactly overlapped with the whole emission region of UCNPs. The whole emission region decreased, indicating the efficient energy transfer from UCNPs to BPQDs. The measured upconversion luminescence decay curves at 662 nm ($^4F_{9/2} \rightarrow {}^4I_{15/2}$ transition) of UCNPs and UCNPs@BPQDs under 808 nm laser excitation (Figure 3c) showed the main component of the lifetimes decrease from 0.59 to 0.47 ms, further confirming the energy transfer process.[37]

DOI: 10.31635/ccschem.019.20180033
CCS Chem. **2019**, *1*, 490–501

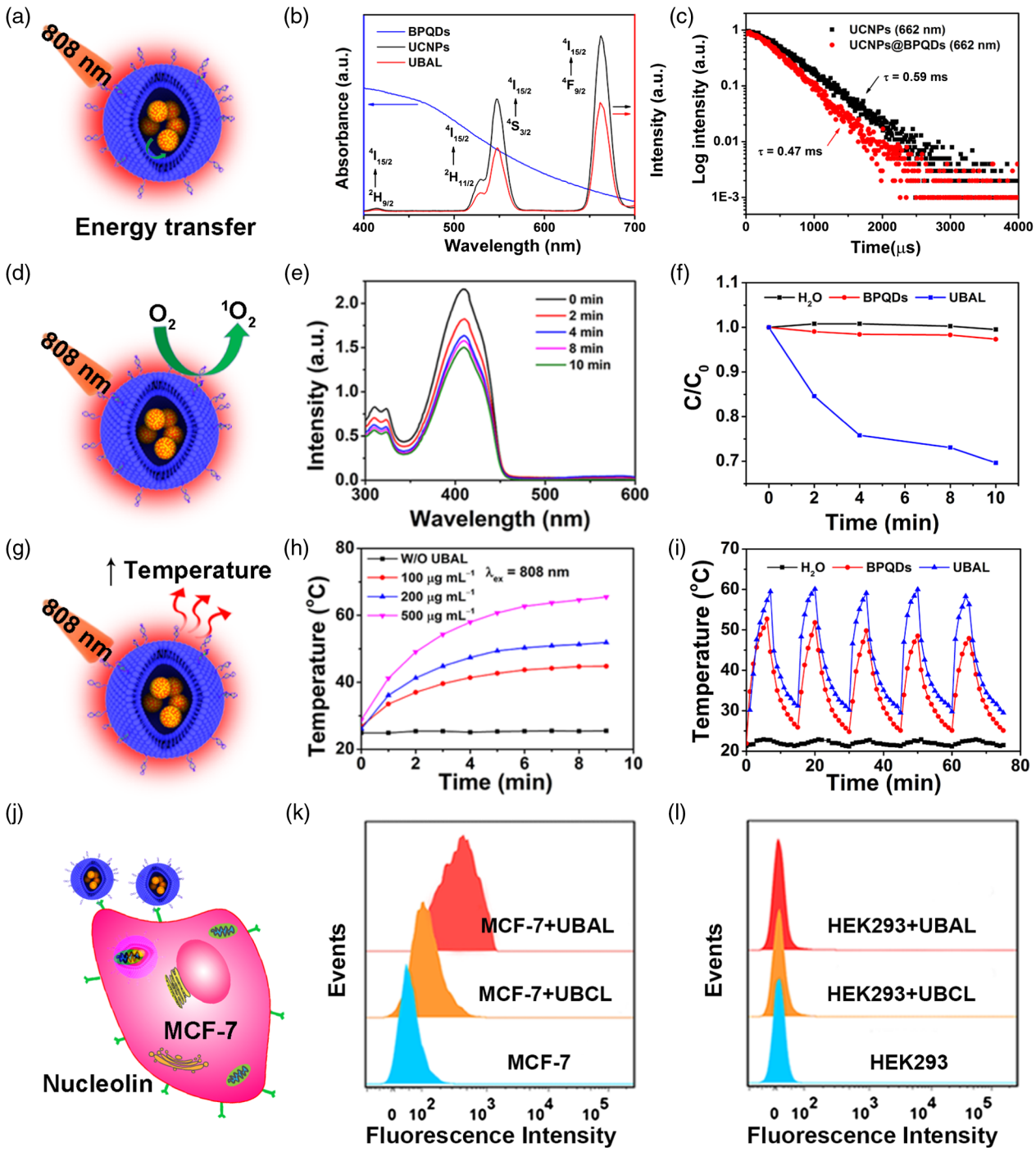

Figure 3 | *Photoresponse performance and selective recognition function of UBAL protocells. (a) The schematic illustration of upconversion luminescence properties and the upconversion resonance energy transfer of UBAL. (b) The UV–vis spectra of BPQDs (blue line), and the upconversion spectrum of UCNPs (black line) and UBAL (red line). (c) Decay curves from $^4F_{9/2}$ of Er^{3+} obtained by monitoring the emission at wavelengths of 662 nm. (d) The schematic illustration of the $^1O_2$ generation of UBAL under NIR irradiation. (e) Time-course of $^1O_2$ generation by UBAL detected via bleaching of DPBF absorption at 410 nm under 808 nm laser (1.5 W·cm^{-2}) irradiation. (f) Decrease in absorbance intensity of DPBF at 410 nm of BPQDs and UBAL solution under 808 nm laser (1.5 W·cm^{-2}) irradiation. (g) The schematic illustration of heating produced by UBAL under 808 nm laser (1.5 W·cm^{-2}). (h) Photothermal curves of UBAL at different concentrations. (i) Photostability of BPQDs and UBAL under five laser on/off cycles. (j) Illustration of targeting of MCF-7 cells with UBAL. (k, l). Flow cytometry analysis of MCF-7 and HEK293 cells after incubation with FAM-labeled UBAL, with an emission signal evolving from the FAM-labeled on UBAL.*

DOI: 10.31635/ccschem.019.20180033
CCS Chem. **2019**, *1*, 490–501

The UBAL protocells could generate $^1O_2$ under NIR irradiation due to the efficient energy transfer from UCNPs to BPQDs (Figure 3d). As shown in Figure 3e, the absorbance of $^1O_2$-sensitive probe 1,3-diphenylisobenzofuran (DPBF) displays a continuous decrease around 410 nm with the increase of irradiation time, indicating the efficient generation of $^1O_2$ by the UBAL protocells. When UBAL was irradiated for 10 min, the absorption decreased by ~ 30%, demonstrating the efficient energy transfer from UCNPs to BPQDs. As a control, the dependence of DPBF absorbance on the different time of BPQDs excited by 808 nm laser was examined. As shown in Figure 3f, the change in absorption was negligible when the solution of BPQDs in H_2O was illuminated with NIR light. All of our results thus far indicate that the upconversion emission of UBAL protocells from NIR to visible light had potent catalytic activity, leading to decomposition of DPBF[36,38,54] and inducing generation of $^1O_2$ throughout the energy transfer process. In other words, UBAL protocells with NIR-light-harvesting function could efficiently convert light energy into chemical energy.

Notably, the prominent extinction coefficient of BPQDs (~ 14.8 $Lg^{-1}\cdot cm^{-1}$) at 808 nm, which corresponds to a NIR photothermal conversion efficiency of 28.4%, presents BPQDs within UBAL protocells as ideal photothermal agents (Figure 3g).[39] Figure 3h shows a concentration-dependent heating effect, in which 500 $\mu g\cdot mL^{-1}$ UBAL application led to an apparent temperature increase from 28 to 49 °C after 2 min illumination of NIR. In contrast, the temperature increased only by 0.6 °C for UBAL-free solution under the same conditions, indicating that the photoresponsive UBAL protocells could exhibit excellent photothermal responses under NIR irradiation. Figure 3i further shows that the photothermal effect of the UBAL does not undergo deterioration during temperature elevation, suggesting good photothermal stability of UBAL protocells. To investigate the cause of the heating effect attributed to upconverting 808 nm laser to visible light and the possible absorption by BPQD or purely BPQD absorption in our UBAL system, the heating effects generated by UCNPs under 808 nm excitation and BPQDs under commercial LED lights (1000 lm) were measured and compared (Supporting Information Figure S17). Both UCNPs and BPQDs solutions rose < 10 °C within 30 min under the corresponding laser excitation, consistent with several literature reports.[36,55,56] Therefore, our above results confirmed that the thermal effect in the UBAL protocells has three origins: the first is from the UCNPs solution, the second is from BPQDs absorbing the converted visible light to generate extra heat, and the third is from BPQDs excited by an 808 nm laser. Furthermore, the thermal effect of UBAL was derived primarily from the heat absorption of BPQDs. All of these results demonstrated that UBAL protocells efficiently convert NIR-light energy into chemical and heat energy.

The UBAL protocells also possess strong binding affinity and high selectivity toward their targets due to the surface-anchored aptamers (Figure 3j), revealed by employing a nucleolin-specific aptamer, AS1411, model in this study. We achieved the aptamer functionalization by covalent attachment to the surface of liposomes utilizing thiol-maleimide cross-linking chemistry between 3′-thiol-modified aptamer and Mal-Lip.[57] It was necessary to characterize the conjugation yield of aptamer onto UBAL protocells before verifying the binding affinity between the aptamer and the liposome; a critical step in assessing reproducibility and quality control of our UBAL protocells. To characterize the coupling efficiency and calculate the distribution density of aptamers on the surface of liposomes, a standard curve (I–$C_{FAM\text{-}Apt}$) was determined by measuring the fluorescence intensity of different concentrations of FAM-Apt (Supporting Information Figure S18). Approximately 750.4 μM aptamer was attached to the surface of the liposome per milliliter protostome solution, which corresponded to a coupling efficiency of 71.93% and was calculated to be ~ 59 aptamer molecules per one liposome, which is expected to lead to a strong binding affinity.

Consequently, the strong binding affinity and good selectivity of UBAL protocells toward their targets were characterized by flow cytometry and confocal microscopy. As shown in Figure 3k, a massive fluorescence peak shift was apparent for MCF-7 (human breast cancer) cells incubated with the FAM-labeled UBAL, clearly indicating the strong binding affinity of the UBAL to target cells. Meanwhile, FAM-labeled UCNPs@BPQDs@Ctrl-Lip (UBCL) exhibited weak affinity to MCF-7 cells, evidenced by a small shift in the fluorescence peak. In contrast, a fluorescence peak shift was not observed after incubating UBAL or UBCL with HEK293 (human embryonic kidney) cells (Figure 3l), signifying that UBAL protocells have much stronger binding affinity to MCF-7 cells compared with the noncancer cell line, HEK293. The targeting specificity of UBAL toward MCF-7 cells was also confirmed by confocal microscopy (Supporting Information Figure S19). A strong emission signal was detected from MCF-7 cells surface after incubation with UBAL. Overlay of dark- and bright-field images showed that the signal was primarily within the cytoplasm, indicating aptamer-guided binding of the UBAL to MCF-7 cells. In contrast, no evident emission signal was observed in MCF-7 cells treated with our UBCL control. Thus, the excellent cell-targeting capability of UBAL protocells was assumed to have improved the efficiency of light-energy conversion at the target tissue.

Detection of intracellular $^1O_2$ generation and photothermal response

With both good light-energy conversion and cell-targeting capability, the performance of the UBAL protocells in

DOI: 10.31635/ccschem.019.20180033
CCS Chem. **2019**, *1*, 490–501

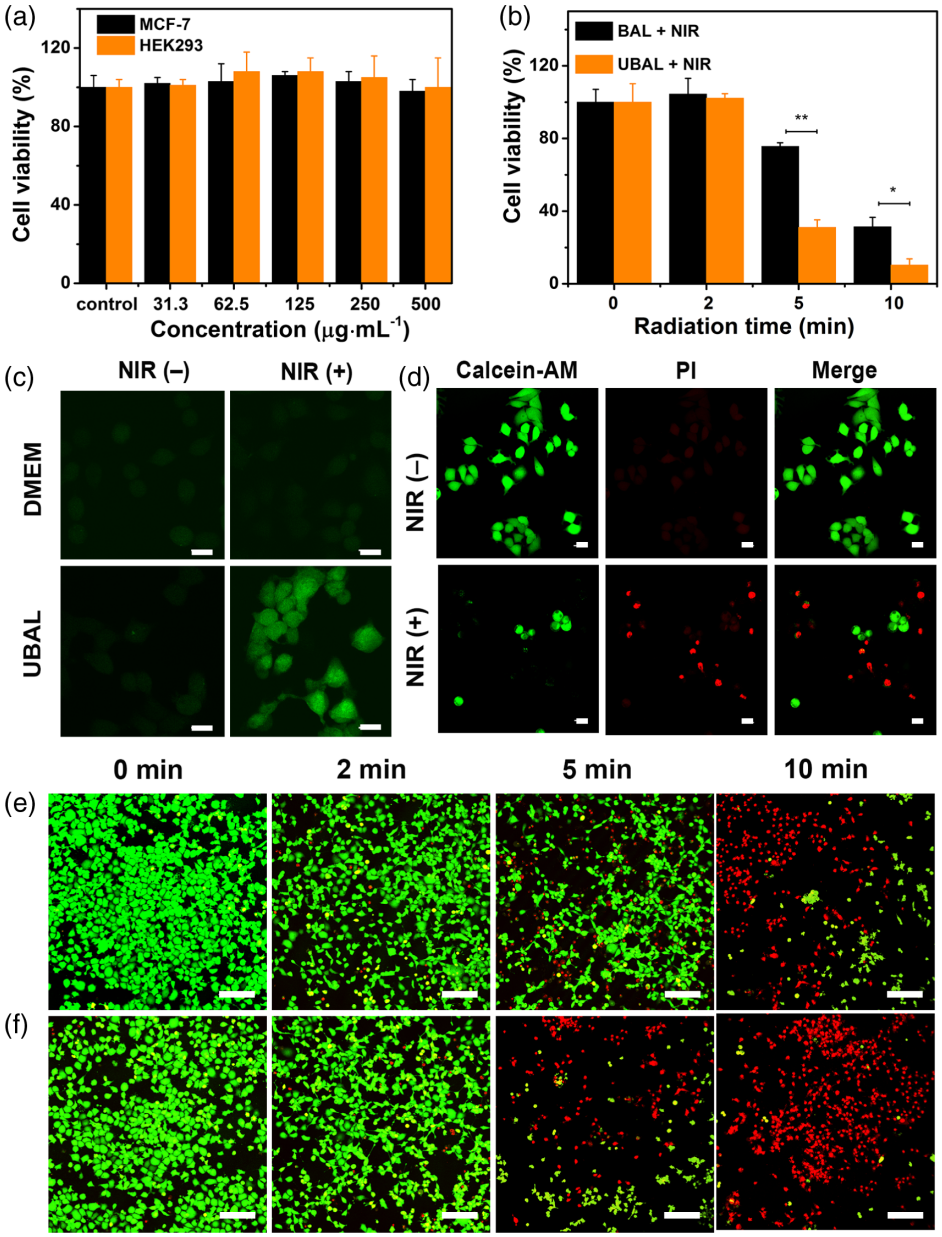

Figure 4 | *UBAL protocells usage for in vitro targeted photodynamic/photothermal therapy. (a) Cell viability of MCF-7 and HEK293 cells with various concentrations of UBAL. (b) Relative viability of MCF-7 cells after incubation with BAL and UBAL at different irradiation time. **P < 0.01. Data are presented as the mean ± SD (*P < 0.05, **P < 0.01). (c) The intracellular $^1O_2$ production under different treatments, using H_2DCFH-DA as a probe. Scale bars, 20 μm. (d) Fluorescence images of MCF-7 cells pretreated with the antioxidant AA for 1 h before UBAL treatment without or with NIR irradiation. Scale bars, 20 μm. (e, f) Confocal fluorescence images of MCF-7 cells treated with BAL or UBAL after different times of NIR irradiation, stained with calcein-AM (live cells, green fluorescence) and PI (dead cells, red fluorescence). Scale bars, 100 μm.*

targeted combined photodynamic and photothermal therapy was evaluated. Figure 4a and Supporting Information Figure S20 show that the UBAL protocells displayed excellent biocompatibility. The intracellular $^1O_2$ generated by the UBAL protocells under NIR-light illumination was determined with a standard fluorescent indicator 2′,7′-dichlorodihydrofluorescein diacetate (H_2DCFH-DA). As shown in Figure 4c and Supporting Information Figure S21, MCF-7 cells treated with UBAL together with NIR irradiation displayed strong fluorescence, suggesting that UBAL might have produced reactive oxygen species (ROS) inside MCF-7 breast cancer cells.

Furthermore, the intracellular photothermal response of UBAL was evaluated with the fluorescent live/dead assay. $^1O_2$ generated by UBAL under NIR irradiation

DOI: 10.31635/ccschem.019.20180033
CCS Chem. **2019**, *1*, 490–501

caused cellular apoptosis and affected the photothermal response signals of the live/dead assay. This observation was made by pretreatment of the MCF-7 cells with 1 mM of the antioxidant, ascorbic acid (AA), for 1 h prior to UBAL treatment to scavenge ROS. Figure 4d and Supporting Information Figure S22 show MCF-7 cells treated with UBAL alone (sham) and MCF-7 cells treated with UBAL and NIR-light irradiation (test). The sham and the test cells were stained with calcein-AM to determine cell viability and with propidium iodide (PI) to detect dead cells. For the UBAL-treated sham, both the cytoplasm and nucleus predominantly stained with calcein-AM and showed negligible PI staining, demonstrating pronounced cell viability. On the other hand, the UBAL-treated and NIR-light-irradiated test cells displayed very low levels of calcein-AM staining and predominantly high PI staining, which likely resulted from the good photothermal response of UBAL following NIR-light irradiation and a significant increase in cell membrane permeability and subsequent cell death.

Inspired by these exciting results, the combined therapy of UBAL was examined in vitro over a time course, using UBAL protocells prototype, BPQDs@Apt-Lip (BAL), as control. 3-(4,5-dimethylthiazol-2-yl)-5-(3-carboxymethoxyphenyl)-2-(4-sulfophenyl)-2H-tetrazolium (MTS) assay (Figure 4b) together with live/dead assay (Figure 4e, f) were performed to evaluate the photodynamic and photothermal synergistic therapeutic efficacy. NIR laser effect was first excluded by examining the viability of MCF-7 cells irradiated by an 808 nm laser (Supporting Information Figure S23). No significant decrease in cell viability was observed, indicating that NIR irradiation in the absence of UBAL protocells did not compromise cell viability. The viabilities of MCF-7 cells incubated with BAL or UBAL under 808 nm irradiation (1.5 W·cm^{-2}) show a downward trend as irradiation time increases. In

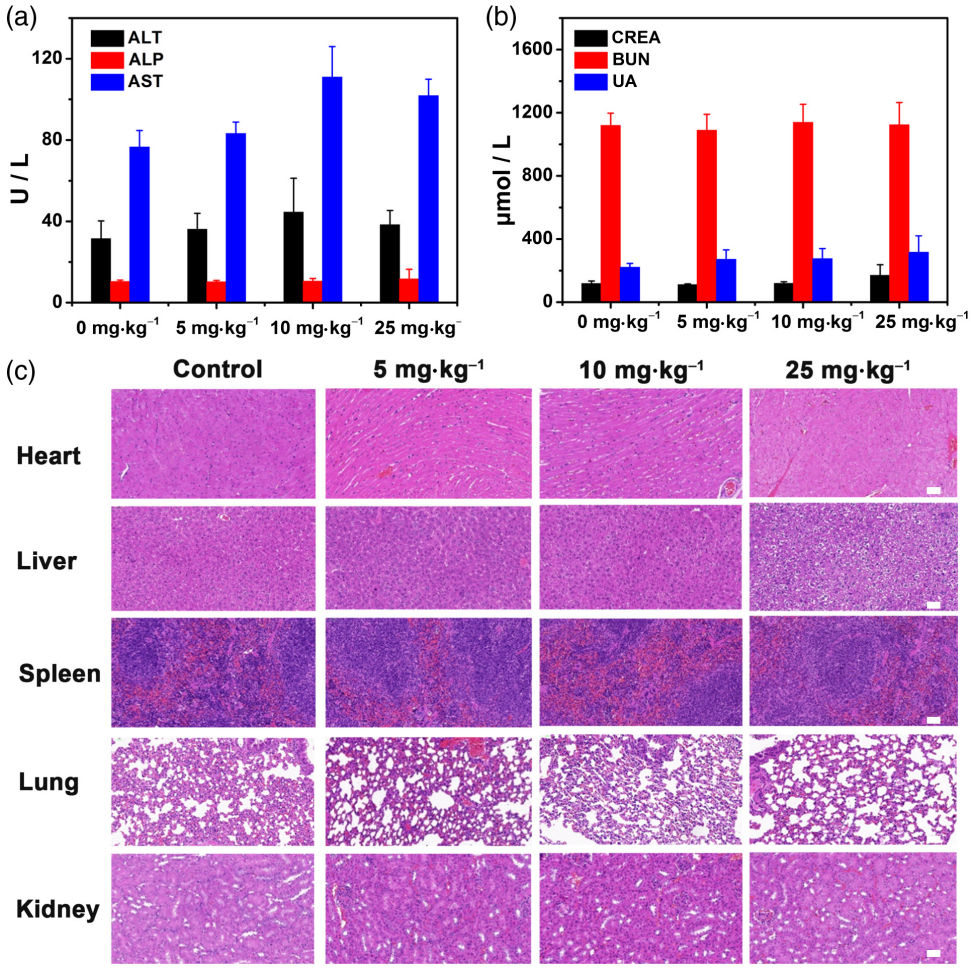

Figure 5 | *Long-term (30 days) in vivo toxicity studies of UBAL protocells. (a) The blood levels of alanine aminotransferase, alkaline phosphatase, and aspartate aminotransferase from control and treated mice as liver function markers. (b) Creatinine, blood urea nitrogen, and uric acid levels in the blood representing kidney functions. (c) Histological examinations of major organs (heart, liver, spleen, lung, and kidney) of intravenous injection groups at different doses of UBAL protocells. Scale bar, 200 μm.*

DOI: 10.31635/ccschem.019.20180033
CCS Chem. **2019**, *1*, 490–501

comparison, cell death rate in UBAL treatment group is significantly higher than that in the BAL treatment group, indicating UBAL protocells offer the most effective cancer cell killing. The results of our cell live/dead assays also demonstrate that almost all cells were killed when the cells were treated with UBAL under 808 irradiation for 10 min, highlighting the significance of the therapeutic effect of NIR-responsive UBAL protocells. All of our results indicate that the photoresponsive protocells possess powerful potential for the combined photodynamic and photothermal therapeutic efficiency.

In vivo biocompatibility evaluation

The in vivo targeted photodynamic and photothermal therapy performance of UBAL protocells was studied in sequence, as follows: In vivo, the biocompatibility was investigated to facilitate the potential clinical translation of the UBAL protocells. Mice were untreated or treated with UBAL. The bodyweights of healthy mice were recorded during 1 month feeding, and the mice were euthanased; blood was drawn from each mouse before they were sacrificed. Biopsies from the major organs (heart, liver, spleen, lung, and kidney) were evaluated by

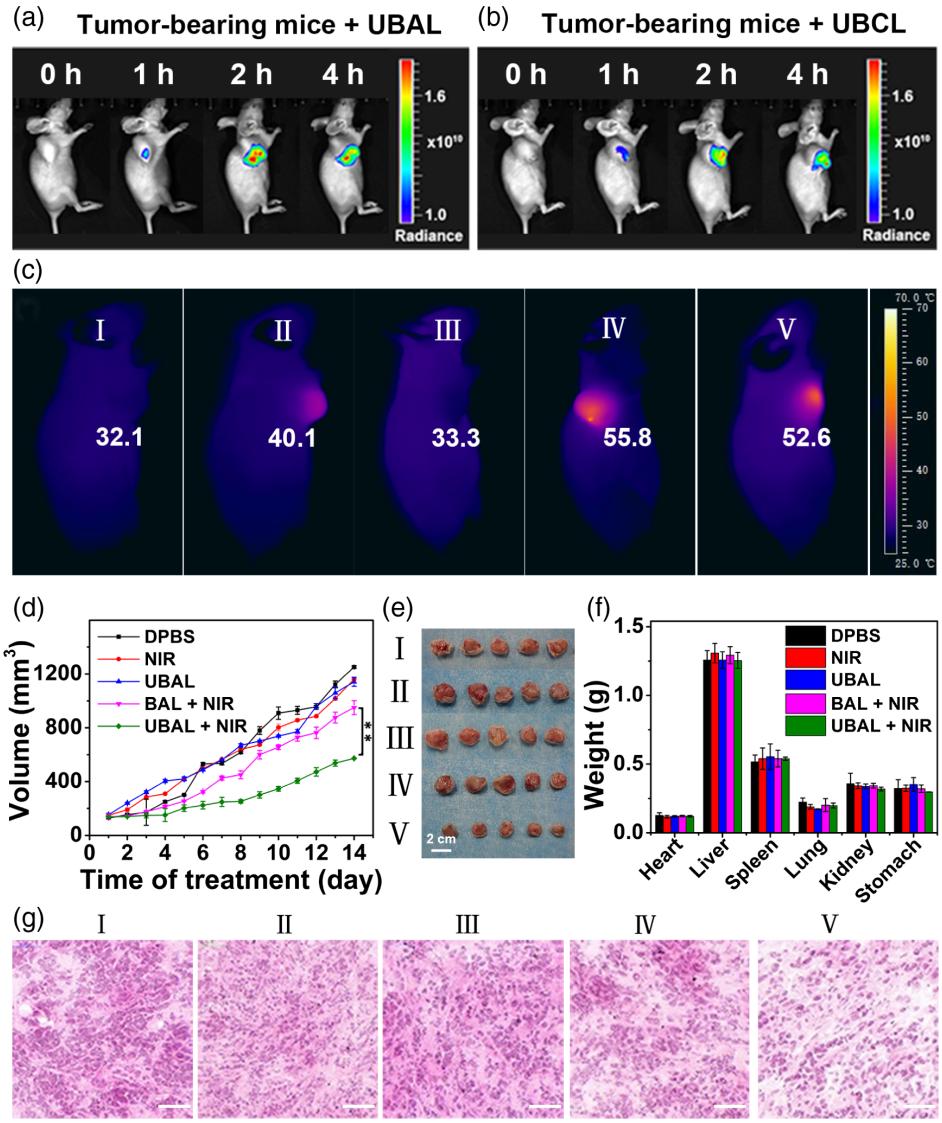

Figure 6 | *In vivo UCL images and the evaluation of therapeutic efficacy. Time-dependent UCL images of 4T1 tumor-bearing mice after intravenous injection of (a) UBAL and (b) UBCL. (c) Infrared thermal images of tumor sites after injecting specific samples under the 808 nm laser irradiation (1.5 W·cm^{-2}). (d) Volume curves of tumor growth. (e) Photos of the final tumors harvested from sacrificed mice. (f) The average weight of organs (heart, liver, spleen, lung, kidney, and stomach) collected from mice. (g) Micrographs of H&E-stained tumor tissue. Group I, DPBS; Group II, NIR; Group III, UBAL; Group IV, BAL + NIR; Group V, UBAL + NIR. Scale bar, 200 μm.*

DOI: 10.31635/ccschem.019.20180033
CCS Chem. **2019**, *1*, 490–501

hematoxylin and eosin (H&E) staining. As can be seen in Supporting Information Figure S24, no significant difference in weight change are apparent between the control- and UBAL-treated groups. Additionally, blood biochemistry and hematology examinations (Figure 5a,b and Supporting Information Figure S25) showed that the liver function, kidney function, and blood indices of mice injected with the UBAL had no significant differences or abnormities compared with the control group. Moreover, the tissues of the major organs had no obvious pathological abnormity compared with the control mice, implying high histocompatibility of UBAL protocells (Figure 5c). These results demonstrate that UBAL protocells possess high biocompatibility.

In vivo time-dependent UCL imaging and therapeutic efficacy

In order to investigate the tumor-specific accumulation capability of UBAL in vivo, UCL imaging was used to track the photoresponsive protocells. When UBAL was injected through the tail vein into female Balb/c mice bearing 4T1 tumor, the fluorescence signal could be seen at the tumor site, and the signal intensity reached a maximum at 2 h. In contrast, the signal intensity was dimmer and disappeared more rapidly in mice injected with UBCL (Figure 6a,b and Supporting Information Figure S26), suggesting that UBAL possessed better tumor accumulation capability than UBCL. Furthermore, female Balb/c mice bearing subcutaneous 4T1 tumors were divided randomly into five groups ($n = 5$) and treated with different agents: Group I mice were injected with DPBS; Group II mice were exposed to NIR irradiation; Group III mice were injected with UBAL; Group IV mice were injected with BAL and exposed to NIR irradiation (BAL + NIR); Group V mice were injected with UBAL and exposed to NIR irradiation (UBAL + NIR). As presented in Figure 6c, acquired thermal imaging data show that the tumor temperature in Groups IV and V treated mice rose rapidly to 50 °C and displayed the most severe burn at the tumor region compared with Groups I–III indicating that the high-tumor targeting of BAL and UBAL generated significant photothermal conversion under NIR-light illumination. In addition, compared with the Groups I–IV, Group V mice treated with UBAL protocells and NIR light displayed the slowest increase of tumor volume (Figure 6d), confirming the good antitumor efficacy with photodynamic/photothermal therapy of the NIR-light-regulated UBAL protocells. The tumors from the sacrificed mice were collected, and the average weight of the isolated major organs (heart, liver, spleen, lung, kidney, and stomach) was recorded. As shown in Figure 6e, tumors isolated from mice in Group V had the smallest volume, thus demonstrating that the NIR-light-regulated UBAL efficiently inhibited tumor growth. Each type of mice and isolated organ from mice in the five groups showed similar weights, as presented in Figure 6e and Supporting Information Figure S27, further confirming good biocompatibility of the UBAL protocells. The histological changes of major organs and tumor tissues were also examined by H&E staining. The main organs (kidney, liver, and spleen) of the mice in the five groups displayed no prominent abnormalities or lesions (Supporting Information Figure S28), while the tumor tissues (Figure 6g) exhibited irregular widening of the intercellular space in Group V mice, indicating that the NIR-light-regulated UBAL protocells were effective in damaging the tumor tissue.

Conclusion

We have fabricated artificial photoresponsive protocells that mimic the structure and light-energy conversion function of photosynthetic bacteria. These artificial protocells were further applied in NIR-light-regulated photodynamic and photothermal therapy. Under NIR stimulation, the protocells could efficiently convert the energy of incident photons into chemical energy and heat. Due to the efficient generation of $^1O_2$ and heat under irradiation, the photoresponsive protocells displayed high performance in ablating tumor cells and suppressing the growth of solid tumors. This work not only provides a new approach for fabricating light-harvesting systems with potential applications in biomedicine and bioelectronics, but also open new possibilities for constructing intelligent systems that rival living organisms.

Supporting Information

Supporting Information is available.

Conflict of Interest

The authors declare no competing financial interests.

Acknowledgments

This work was supported by the National Key R&D Program of China (2017YFA0208000), the National Natural Science Foundation of China (21675120 and 31701249), the Foundation for Innovative Research Groups of NSFC (grant 21521063), and the Keypoint Research and Invention Program of Hunan province (2017DK2011).

References

1. Studart, A. R. Towards High-Performance Bioinspired Composites. *Adv. Mater.* **2012**, *24*, 5024–5044.

2. Zhao, N.; Wang, Z.; Cai, C.; Shen, H.; Liang, F.; Wang, D.; Wang, C.; Zhu, T.; Guo, J.; Wang, Y.; Liu, X.; Duan, C.; Wang, H.; Mao, Y.; Jia, X.; Dong, H.; Zhang, X.; Xu, J. Bioinspired Materials: From Low to High Dimensional Structure. *Adv. Mater.* **2014**, *26*, 6994–7017.
3. Zhao, Y.; Sakai, F.; Su, L.; Liu, Y.; Wei, K.; Chen, G.; Jiang, M. Progressive Macromolecular Self-Assembly: From Biomimetic Chemistry to Bio-Inspired Materials. *Adv. Mater.* **2013**, *25*, 5215–5256.
4. Zan, G.; Wu, Q. Biomimetic and Bioinspired Synthesis of Nanomaterials/Nanostructures. *Adv. Mater.* **2016**, *28*, 2099–2147.
5. Montero de Espinosa, L.; Meesorn, W.; Moatsou, D.; Weder, C. Bioinspired Polymer Systems With Stimuli-Responsive Mechanical Properties. *Chem. Rev.* **2017**, *117*, 12851–12892.
6. Takahashi, R.; Kobuke, Y. Hexameric Macroring of Gable-Porphyrins as a Light-Harvesting Antenna Mimic. *J. Am. Chem. Soc.* **2002**, *125*, 2372–2373.
7. Huh, J.; Saikin, S. K.; Brookes, J. C.; Valleau, S.; Fujita, T.; Aspuru-Guzik, A. Atomistic Study of Energy Funneling in the Light-Harvesting Complex of Green Sulfur Bacteria. *J. Am. Chem. Soc.* **2014**, *136*, 2048–2057.
8. Orf, G. S.; Blankenship, R. E. Chlorosome Antenna Complexes From Green Photosynthetic Bacteria. *Photosynth. Res.* **2013**, *116*, 315–331.
9. Hanke, T.; Cesar, J.; Knittel, V.; Trügler, A.; Hohenester, U.; Leitenstorfer, A.; Bratschitsch, R. Tailoring Spatiotemporal Light Confinement in Single Plasmonic Nanoantennas. *Nano Lett.* **2012**, *12*, 992–996.
10. Scholes, G. D.; Fleming, G. R.; Olaya-Castro, A.; van Grondelle, R. Lessons From Nature About Solar Light Harvesting. *Nat. Chem.* **2011**, *3*, 763–774.
11. Hildner, R.; Brinks, D.; Nieder, J. B.; Cogdell, R. J.; van Hulst, N. F. Quantum Coherent Energy Transfer Over Varying Pathways in Single Light-Harvesting Complexes. *Science* **2013**, *340*, 1448.
12. Ziessel, R.; Harriman, A. Artificial Light-Harvesting Antennae: Electronic Energy Transfer by Way of Molecular Funnels. *Chem. Commun.* **2011**, *47*, 611–631.
13. Grätzel, M. Dye-Sensitized Solar Cells. *J. Photochem. Photobiol., C* **2003**, *4*, 145–153.
14. Zarick, H. F.; Erwin, W. R.; Boulesbaa, A.; Hurd, O. K.; Webb, J. A.; Puretzky, A. A.; Geohegan, D. B.; Bardhan, R. Improving Light Harvesting in Dye-Sensitized Solar Cells Using Hybrid Bimetallic Nanostructures. *ACS Photonics* **2016**, *3*, 385–394.
15. Liu, Z. E.; Wang, J.; Li, Y.; Hu, X.; Yin, J.; Peng, Y.; Li, Z.; Li, Y.; Li, B.; Yuan, Q. Near-Infrared Light Manipulated Chemoselective Reductions Enabled by an Upconversional Supersandwich Nanostructure. *ACS Appl. Mater. Interfaces* **2015**, *7*, 19416–19423.
16. Li, X. B.; Gao, Y. J.; Wang, Y.; Zhan, F.; Zhang, X. Y.; Kong, Q. Y.; Zhao, N. J.; Guo, Q.; Wu, H. L.; Li, Z. J.; Tao, Y.; Zhang, J. P.; Chen, B.; Tung, C. H.; Wu, L. Z. Self-Assembled Framework Enhances Electronic Communication of Ultrasmall-Sized Nanoparticles for Exceptional Solar Hydrogen Evolution. *J. Am. Chem. Soc.* **2017**, *139*, 4789–4796.
17. Pellet, N.; Gao, P.; Gregori, G.; Yang, T. Y.; Nazeeruddin, M. K.; Maier, J.; Gratzel, M. Mixed-Organic-Cation Perovskite Photovoltaics for Enhanced Solar-Light Harvesting. *Angew. Chem. Int. Ed. Engl.* **2014**, *53*, 3151–3157.
18. Li, Y.; Di, Z.; Gao, J.; Cheng, P.; Di, C.; Zhang, G.; Liu, B.; Shi, X.; Sun, L. D.; Li, L.; Yan, C. H. Heterodimers Made of Upconversion Nanoparticles and Metal–Organic Frameworks. *J. Am. Chem. Soc.* **2017**, *139*, 13804–13810.
19. Tobin, E. M. Photochrome-Mediated Regulation of Messenger RNAs for the Small Subunit of Ribulose 1,5-Bisphosphate Carboxylase and the Light-Harvesting Chlorophyll a/b-Protein in Lemna gibba. *Plant Mol. Biol.* **1981**, *1*, 35–51.
20. Lu, K.; He, C.; Lin, W. A Chlorin-Based Nanoscale Metal–Organic Framework for Photodynamic Therapy of Colon Cancers. *J. Am. Chem. Soc.* **2015**, *137*, 7600–7603.
21. Park, J.; Jiang, Q.; Feng, D.; Mao, L.; Zhou, H. C. Size-Controlled Synthesis of Porphyrinic Metal–Organic Framework and Functionalization for Targeted Photodynamic Therapy. *J. Am. Chem. Soc.* **2016**, *138*, 3518–3525.
22. Orf, G. S.; Collins, A. M.; Niedzwiedzki, D. M.; Tank, M.; Thiel, V.; Kell, A.; Bryant, D. A.; Montano, G. A.; Blankenship, R. E. Polymer-Chlorosome Nanocomposites Consisting of Non-Native Combinations of Self-Assembling Bacteriochlorophylls. *Langmuir* **2017**, *33*, 6427–6438.
23. Croce, R.; van Amerongen, H. Natural Strategies for Photosynthetic Light Harvesting. *Nat. Chem. Biol.* **2014**, *10*, 492–501.
24. Wasielewski, M. R. Self-Assembly Strategies for Integrating Light Harvesting and Charge Separation in Artificial Photosynthetic Systems. *Acc. Chem. Res.* **2009**, *42*, 1910–1921.
25. Huang, J.; Antonietti, M.; Liu, J. Bio-Inspired Carbon Nitride Mesoporous Spheres for Artificial Photosynthesis: Photocatalytic Cofactor Regeneration for Sustainable Enzymatic Synthesis. *J. Mater. Chem. A* **2014**, *2*, 7686–7693.
26. Xue, B.; Li, Y.; Yang, F.; Zhang, C.; Qin, M.; Cao, Y.; Wang, W. An Integrated Artificial Photosynthesis System Based on Peptide Nanotubes. *Nanoscale* **2014**, *6*, 7832–7837.
27. Wang, J.-J.; Wang, J.; Feng, K.; Zhang, H.-H.; Li, Z.-J.; Liu, B.; Tung, C.-H.; Wu, L.-Z. Enhanced Visible-Light-Driven Hydrogen Generation by in Situ Formed Photocatalyst RGO–CdS–Ni_xS from Metal Salts and RGO–CdS Composites. *J. Mater. Chem. A* **2017**, *5*, 9537–9543.
28. Wang, S.; Li, M.; Patil, A. J.; Sun, S.; Tian, L.; Zhang, D.; Cao, M.; Mann, S. Design and Construction of Artificial Photoresponsive Protocells Capable of Converting Day Light to Chemical Energy. *J. Mater. Chem. A* **2017**, *5*, 24612–24616.
29. Jin, S.; Son, H. J.; Farha, O. K.; Wiederrecht, G. P.; Hupp, J. T. Energy Transfer From Quantum Dots to Metal–Organic Frameworks for Enhanced Light Harvesting. *J. Am. Chem. Soc.* **2013**, *135*, 955–958.
30. Pu, F.; Wu, L.; Ran, X.; Ren, J.; Qu, X. G-Quartet-Based Nanostructure for Mimicking Light-Harvesting Antenna. *Angew. Chem. Int. Ed. Engl.* **2015**, *54*, 892–896.
31. Ahn, T. K.; Avenson, T. J.; Ballottari, M.; Cheng, Y.-C.; Niyogi, K. K.; Bassi, R.; Fleming, G. R. Architecture of a

Charge-Transfer State Regulating Light Harvesting in a Plant Antenna Protein. *Science* **2008**, *320*, 794.
32. Li, X.-P.; Björkman, O.; Shih, C.; Grossman, A. R.; Rosenquist, M.; Jansson, S.; Niyogi, K. K. A Pigment-Binding Protein Essential for Regulation of Photosynthetic Light Harvesting. *Nature* **2000**, *403*, 391.
33. D'souza, F.; Maligaspe, E.; Ohkubo, K.; Zandler, M. E.; Subbaiyan, N. K.; Fukuzumi, S. Photosynthetic Reaction Center Mimicry: Low Reorganization Energy Driven Charge Stabilization in Self-Assembled Cofacial Zinc Phthalocyanine Dimer–Fullerene Conjugate. *J. Am. Chem. Soc.* **2009**, *131*, 8787–8797.
34. Seibert, M.; Picorel, R.; Rubin, A. B.; Connolly, J. S. Spectral, Photophysical, and Stability Properties of Isolated Photosystem II Reaction Center. *Plant Physiol.* **1988**, *87*, 303.
35. Lukashev, E. P.; Knox, P. P.; Gorokhov, V. V.; Grishanova, N. P.; Seifullina, N. K.; Krikunova, M.; Lokstein, H.; Paschenko, V. Z. Purple-Bacterial Photosynthetic Reaction Centers and Quantum-Dot Hybrid-Assemblies in Lecithin Liposomes and Thin Films. *J. Photochem. Photobiol., B* **2016**, *164*, 73–82.
36. Wang, H.; Yang, X.; Shao, W.; Chen, S.; Xie, J.; Zhang, X.; Wang, J.; Xie, Y. Ultrathin Black Phosphorus Nanosheets for Efficient Singlet Oxygen Generation. *J. Am. Chem. Soc.* **2015**, *137*, 11376–11382.
37. Lv, R.; Yang, D.; Yang, P.; Xu, J.; He, F.; Gai, S.; Li, C.; Dai, Y.; Yang, G.; Lin, J. Integration of Upconversion Nanoparticles and Ultrathin Black Phosphorus for Efficient Photodynamic Theranostics Under 808 nm Near-Infrared Light Irradiation. *Chem. Mater.* **2016**, *28*, 4724–4734.
38. Li, Y.; Liu, Z.; Hou, Y.; Yang, G.; Fei, X.; Zhao, H.; Guo, Y.; Su, C.; Wang, Z.; Zhong, H.; Zhuang, Z.; Guo, Z. Multifunctional Nanoplatform Based on Black Phosphorus Quantum Dots for Bioimaging and Photodynamic/Photothermal Synergistic Cancer Therapy. *ACS Appl. Mater. Interfaces* **2017**, *9*, 25098–25106.
39. Sun, Z.; Xie, H.; Tang, S.; Yu, X. F.; Guo, Z.; Shao, J.; Zhang, H.; Huang, H.; Wang, H.; Chu, P. K. Ultrasmall Black Phosphorus Quantum Dots: Synthesis and Use as Photothermal Agents. *Angew. Chem. Int. Ed. Engl.* **2015**, *54*, 11526–11530.
40. Shao, J.; Xie, H.; Huang, H.; Li, Z.; Sun, Z.; Xu, Y.; Xiao, Q.; Yu, X. F.; Zhao, Y.; Zhang, H.; Wang, H.; Chu, P. K. Biodegradable Black Phosphorus-Based Nanospheres for in Vivo Photothermal Cancer Therapy. *Nat. Commun.* **2016**, *7*, 12967.
41. Chen, W.; Ouyang, J.; Liu, H.; Chen, M.; Zeng, K.; Sheng, J.; Liu, Z.; Han, Y.; Wang, L.; Li, J.; Deng, L.; Liu, Y. N.; Guo, S. Black Phosphorus Nanosheet-Based Drug Delivery System for Synergistic Photodynamic/Photothermal/Chemotherapy of Cancer. *Adv. Mater.* **2017**, *29*, 1603864.
42. Haase, M.; Schäfer, H. Upconverting Nanoparticles. *Angew. Chem. Int. Ed.* **2011**, *50*, 5808–5829.
43. Wu, X.; Lee, H.; Bilsel, O.; Zhang, Y.; Li, Z.; Chen, T.; Liu, Y.; Duan, C.; Shen, J.; Punjabi, A.; Han, G. Tailoring Dye-Sensitized Upconversion Nanoparticle Excitation Bands Towards Excitation Wavelength Selective Imaging. *Nanoscale* **2015**, *7*, 18424–18428.
44. Zhou, J.; Liu, Q.; Feng, W.; Sun, Y.; Li, F. Upconversion Luminescent Materials: Advances and Applications. *Chem. Rev.* **2015**, *115*, 395–465.
45. Xie, X.; Li, Z.; Zhang, Y.; Guo, S.; Pendharkar, A. I.; Lu, M.; Huang, L.; Huang, W.; Han, G. Emerging ≈800 nm Excited Lanthanide-Doped Upconversion Nanoparticles. *Small* **2017**, *13*, 1602843.
46. Zhu, H.; Nagaoka, Y.; Hills-Kimball, K.; Tan, R.; Yu, L.; Fang, Y.; Wang, K.; Li, R.; Wang, Z.; Chen, O. Pressure-Enabled Synthesis of Hetero-Dimers and Hetero-Rods Through Intraparticle Coalescence and Interparticle Fusion of Quantum-Dot-Au Satellite Nanocrystals. *J. Am. Chem. Soc.* **2017**, *139*, 8408–8411.
47. Liu, K.; Yuan, C.; Zou, Q.; Xie, Z.; Yan, X. Self-Assembled Zinc/Cystine-Based Chloroplast Mimics Capable of Photoenzymatic Reactions for Sustainable Fuel Synthesis. *Angew. Chem. Int. Ed.* **2017**, *56*, 7876–7880.
48. Li, J.; Mo, L.; Lu, C. H.; Fu, T.; Yang, H. H.; Tan, W. Functional Nucleic Acid-Based Hydrogels for Bioanalytical and Biomedical Applications. *Chem. Soc. Rev.* **2016**, *45*, 1410–1431.
49. Meng, H. M.; Liu, H.; Kuai, H.; Peng, R.; Mo, L.; Zhang, X. B. Aptamer-Integrated DNA Nanostructures for Biosensing, Bioimaging and Cancer Therapy. *Chem. Soc. Rev.* **2016**, *45*, 2583–2602.
50. Cheng, L.; Yang, K.; Li, Y. G.; Chen, J. H.; Wang, C.; Shao, M. W.; Lee, S. T.; Liu, Z. Facile Preparation of Multifunctional Upconversion Nanoprobes for Multimodal Imaging and Dual-Targeted Photothermal Therapy. *Angew. Chem. Int. Ed.* **2011**, *50*, 7385–7390.
51. Yao, C.; Wang, P. Y.; Li, X. M.; Hu, X. Y.; Hou, J. L.; Wang, L. Y.; Zhang, F. Near-Infrared-Triggered Azobenzene-Liposome/Upconversion Nanoparticle Hybrid Vesicles for Remotely Controlled Drug Delivery to Overcome Cancer Multidrug Resistance. *Adv. Mater.* **2016**, *28*, 9341–9348.
52. Xie, X.; Gao, N.; Deng, R.; Sun, Q.; Xu, Q. H.; Liu, X. Mechanistic Investigation of Photon Upconversion in $Nd^{(3+)}$-Sensitized Core–Shell nanoparticles. *J. Am. Chem. Soc.* **2013**, *135*, 12608–12611.
53. Ju, Q.; Chen, X.; Ai, F. J.; Peng, D. F.; Lin, X. D.; Kong, W.; Shi, P.; Zhu, G. Y.; Wang, F. An Upconversion Nanoprobe Operating in the First Biological Window. *J. Mater. Chem. B* **2015**, *3*, 3548–3555.
54. Guo, T.; Wu, Y.; Lin, Y.; Xu, X.; Lian, H.; Huang, G.; Liu, J. Z.; Wu, X.; Yang, H. H. Black Phosphorus Quantum Dots With Renal Clearance Property for Efficient Photodynamic Therapy. *Small* **2018**, *14*, 1702815.
55. Li, D.; Lai, W.-Y.; Shao, Q.; Huang, W. Multifunctional $NaYF_4$:Yb^{3+}, Er^{3+}@SiO_2@Au Heterogeneous Nanocomposites for Upconversion Luminescence, Temperature Sensing and Photothermal Conversion. *RSC Adv.* **2017**, *7*, 11491–11495.
56. Shao, Q.; Ouyang, L.; Jin, L.; Jiang, J. Multifunctional Nanoheater Based on $NaGdF_4$:Yb^{3+}, Er^{3+} Upconversion Nanoparticles. *Opt. Express* **2015**, *23*, 30057–30066.
57. Alshaer, W.; Hillaireau, H.; Vergnaud, J.; Ismail, S.; Fattal, E. Functionalizing Liposomes With Anti-CD44 Aptamer for Selective Targeting of Cancer Cells. *Bioconjugate Chem.* **2015**, *26*, 1307–1313.